J|A|C|S
ARTICLES

Published on Web 07/23/2009

Unraveling Atomic Positions in an Oxide Spinel with Two Jahn−Teller Ions: Local Structure Investigation of $CuMn_2O_4$

Daniel P. Shoemaker,* Jun Li, and Ram Seshadri

Materials Department, Materials Research Laboratory, and Department of Chemistry and Biochemistry, University of California, Santa Barbara, California 93106

Received March 17, 2009; E-mail: dshoe@mrl.ucsb.edu

Abstract: At first sight, the quenched tetragonal spinel $CuMn_2O_4$ can be formulated with Cu^{2+} and Mn^{3+}, implying that the tetrahedral site is Jahn−Teller (JT)-active Cu^{2+} and the octahedral site is JT-active Mn^{3+}. High-resolution, high-momentum-transfer neutron scattering analysis suggests that the sample has ∼30% inversion: Mn on the tetrahedral Cu site with compensating Cu on the octahedral site. Reverse Monte Carlo (RMC) analysis of the pair distribution function allows details of metal−oxygen connectivity to be probed in a manner that is significantly on the local rather than the average scale. Bond valence analysis of the RMC supercell reveals that both JT ions disproportionate to higher and lower valence states as a means of avoiding their JT tendency, particularly on the tetrahedral site. The occurrence of Cu^{3+} in particular is suggested for the first time and is supported by X-ray photoelectron spectroscopy data. The bimodal distribution of O−Cu−O bond angles at the tetrahedral site (distinct from what is seen for O−Mn−O bond angles) further reveals a hidden distinction between sites previously considered to be equivalent. Application of total scattering techniques originally developed for highly disordered materials permits the examination of nanoscale crystalline structure with elemental specificity that is not available in traditional reciprocal-space analysis.

Introduction

The oxides La_2CuO_4 and $LaMnO_3$ have been at the heart of great excitement in condensed matter science in the last quarter century, as they are the parent compounds of high-temperature copper oxide superconductors[1] and colossal magnetoresistive (CMR) manganese oxides, respectively.[2,3] A distinguishing feature of these compounds and their derivatives is the cooperative Jahn−Teller (JT) activity of the B-site ions Cu^{2+} and Mn^{3+}. In the CMR case, it is believed that JT phenomena are an important component of the unprecedented behavior displayed.[4]

Poorly defined mixtures of copper and manganese oxides known as hopcalite were first found to be effective oxidizers of CO during World War I.[5] Use of hopcalite powder as a low-temperature oxidizer continues today for respiratory protection, and numerous studies have found that its catalytic activity is a result of a flexible valence in $Cu^{1+/2+}$ and $Mn^{3+/4+}$.[6−8] Since the flexible valence allows for catalytic behavior and only a subset of those valences produce JT distortions, it should be of interest to probe the local structure as an indicator of relevant valence states. These distortions do not necessarily align with each other over long ranges.

Such robust JT systems, even when fully crystallized, are a distinct challenge for traditional diffraction methods. For instance, Rietveld analysis[9] of Bragg profiles provides the *average* lattice spacings of JT compounds, and this results in an accurate representation of all of the bond distances only when the JT distortions are completely cooperative, i.e., strain-coupled with the lattice. When JT-driven bond stretches and the consequent rotations are present only on a *local* scale, their effects can average to zero in the Rietveld analysis. Moreover, while *average* lattice spacings and atomic positions are seemingly determined to within thousandths of an angstrom, pairwise bonding distances can be grossly incorrect.[10] Determining element-specific bond lengths within solid solutions, phosphors, and ferroelectrics has been a significant thrust in X-ray absorption spectroscopy[11−15] and has benefited from the recent advent of real-space total scattering analysis.[16−18]

(1) Bednorz, J. G.; Müller, K. A. *Z. Phys. B.* **1986**, *64*, 189.
(2) Kusters, R.; Singleton, J.; Keen, D. A.; McGreevy, R.; Hayes, W. *Phys. B* **1989**, *155*, 362.
(3) Jin, S.; Tiefel, T. H.; McCormack, M.; Fastnacht, R. A.; Ramesh, R.; Chen, L. H. *Science* **1994**, *264*, 413.
(4) Millis, A. J.; Littlewood, P. B.; Shraiman, B. I. *Phys. Rev. Lett.* **1995**, *74*, 5144.
(5) Lamb, A. B.; Scalione, C. C.; Edgar, G. *J. Am. Chem. Soc.* **1922**, *44*, 738.
(6) Vepřek, S.; Cocke, D. L.; Kehl, S.; Oswald, H. R. *J. Catal.* **1986**, *100*, 250.
(7) Dollimore, D.; Tonge, K. H. *J. Chem. Soc. A* **1970**, 1728.
(8) Jones, C.; Cole, K. J.; Taylor, S. H.; Crudace, M. J.; Hutchings, G. J. *J. Mol. Catal. A* **2009**, *305*, 121.
(9) Rietveld, H. M. *J. Appl. Crystallogr.* **1969**, *2*, 65.
(10) Qiu, X.; Proffen, T.; Mitchell, J. F.; Billinge, S. J. L. *Phys. Rev. Lett.* **2005**, *94*, 177203.
(11) Yoshiasa, A.; Inoue, Y.; Kanamaru, F.; Koto, K. *J. Solid State Chem.* **1990**, *86*, 75.
(12) Mikkelsen, J. C.; Boyce, J. B. *Phys. Rev. Lett.* **1982**, *49*, 1412.
(13) Boyce, J. B.; Mikkelsen, J. C. *Phys. Rev. B* **1985**, *31*, 6903.
(14) Boyce, J. B.; Mikkelsen, J. C. *J. Cryst. Growth* **1989**, *98*, 37.
(15) Pellicer-Porres, J.; Polian, A.; Segura, A.; Munoz-Sanjose, V.; Cicco, A. D.; Traverse, A. *J. Appl. Phys.* **2004**, *96*, 1491.
(16) Petkov, V.; Jeong, I.; Chung, J. S.; Thorpe, M. F.; Kycia, S.; Billinge, S. J. L. *Phys. Rev. Lett.* **1999**, *83*, 4089.
(17) Peterson, P. F.; Proffen, T.; Jeong, I.; Billinge, S. J. L.; Choi, K.; Kanatzidis, M. G.; Radaelli, P. G. *Phys. Rev. B* **2001**, *63*, 165211.
(18) Billinge, S. J. L.; Levin, I. *Science* **2007**, *316*, 561.

10.1021/ja902096h CCC: $40.75

Total scattering techniques, which make use of both the Bragg and diffuse scattering in high-quality data sets, allow for new ways of understanding the JT activity of ions in extended oxides by acquiring the pair distribution function (PDF) concurrently with Bragg diffraction data.[19,20] The complementary data sets allow the usual (e.g., Rietveld) analysis in reciprocal space for long-range average parameters and PDF analysis in real space for local atom−atom pairs from typically 1 to 50 Å, with a real-space resolution on the order of hundredths of an angstrom.[21] The PDF, denoted as $G(r)$, is a representation of all distances r between atom pairs in a material and is equal to the Fourier transform of the total scattering structure factor $S(Q)$, where Q is the reciprocal-space scattering vector:

$$G(r) = \frac{2}{\pi}\int_0^\infty Q[S(Q) - 1]\sin(Qr)\,\mathrm{d}Q \qquad (1)$$

Bond length distributions that are averaged in the bulk can become distinct peaks in the low-r PDF. Recent investigations of JT-distorting oxides (most notably $LaMnO_3$) using the PDF method have found that dynamic JT distortions persist even into the high-temperature phase, above the cooperative JT transition temperature. As a consequence, bonding distances are poorly estimated from the average-structure model and are much better described using the PDF.[8,10]

Early understanding of cooperative JT distortions in spinel compounds can be traced back to the vast body of crystallographic data collected on these systems at the Philips Laboratory in Eindhoven that appears in the literature from the 1930s. Early attempts to rationalize the data were made by Goodenough and Loeb[22] on the basis of a mechanism they called "semicovalent exchange." Dunitz and Orgel[23] recognized the role that the JT theorem[24] plays in determining the distorted octahedral coordination of many Cu^{2+} species, including those in extended compounds like $CsCuCl_3$. They also pointed to the role of the JT theorem in determining the tetragonal structures of Mn^{3+} spinel compounds, including hausmannite, Mn_3O_4, and hetærolite, $ZnMn_2O_4$. Wojtowicz[25] carried the analysis further and examined the high-temperature first-order transformation of JT spinels to the cubic spinel structure. Interestingly, in the case of molecular, tetrahedral Cu^{2+} species such as the $CuCl_4^{2-}$ anion, Felsenfeld[26] approached the problem from the viewpoint of a distortion from the preferred square-planar arrangement of ligands around Cu^{2+} that is driven by Coulombic repulsion between the Cl^- anions. It is accurate to say that not much is known regarding Cu^{2+} in the tetrahedral sites of spinels as drivers of tetragonal distortions.

The recent resurgence of interest in spinel compounds with JT-active ions has been driven by the discovery of magnetoelectric effects in compounds such as Mn_3O_4[27,28] and the formation of complex structural ordering and nanoscale phase separation in mixed Mn^{3+}-containing spinel compounds.[29,30]

In this contribution, we examine the oxide spinel $CuMn_2O_4$, a compound containing both Cu^{2+} and Mn^{3+}. The literature on this compound is extensive and somewhat confusing, in part because it crystallizes with varying degrees of inversion, δ, defined by the chemical formula $Cu_{1-\delta}Mn_\delta[Mn_{2-\delta}Cu_\delta]O_4$. Early work from Sinha et al.[31] first suggested a cubic spinel with all Cu^+ in the tetrahedral site and the octahedral site equally occupied by Mn^{3+} and Mn^{4+}. Buhl[32] pointed out that pure compositions with 1:2 Cu/Mn ratios are tetragonal when formed above 750 °C and become phase-separated into a cubic spinel phase and some parasitic phases when cooled below this temperature. Neutron diffraction studies carried out on samples quenched from 940 °C suggested an inversion $\delta = 0.24(2)$ and a c/a tetragonal ratio of 1.03. The need for water quenching to form tetragonal $CuMn_2O_4$ was confirmed by Robbrecht and Henriet-Iserentant.[33] Numerous groups have carried out magnetic susceptibility, X-ray absorption, and X-ray photoelectron spectroscopy (XPS) studies in an attempt to establish the oxidation states of the ions in $CuMn_2O_4$; these have been summarized in the more recent works of Metz et al.[34] and Gillot et al.[35]

We present structural studies of a quenched $CuMn_2O_4$ sample with an average tetragonal structure in the space group $I4_1/amd$. We used neutron total scattering methods to establish the average structure as obtained from Rietveld analysis as well as the local structure obtained by modeling large supercells, in effect using techniques that are normally employed in establishing the local structure of amorphous materials. Our analysis allows statistical questions regarding coordination and bond valence to be addressed, *even for ions on sites with significant site mixing*. We establish the distorted nature of Cu^{2+} on the tetrahedral site and suggest for the first time the existence of Cu^{3+} on the octahedral site. XPS studies, carried out with greatly improved signal-to-noise ratios and energy resolution in comparison with prior work, are consistent with the assignments made on the basis of bond valence sum (BVS) analysis of the local coordination. One purpose of this work is to establish aspects of the structure of $CuMn_2O_4$, including the fascinating charge disproportionation of Cu^{2+} as a means of obviating its JT tendency, and the nature of the JT distortion on the tetrahedral site. Equally, we use this study to demonstrate the power of modern neutron scattering tools, used in judicious conjunction with the tools of computer simulation, in unraveling structural details in a pathologically complex spinel compound.

Methods

Ceramic pellets of $CuMn_2O_4$ were prepared by grinding stoichiometric amounts of CuO and MnO (99.9%, Aldrich) in an agate mortar and pestle, pressing at 100 MPa, and firing in air at 860 °C for 21 h. For the firing, the pellets were placed on a bed of sacrificial

(19) Egami, T.; Billinge, S. J. L. *Underneath the Bragg Peaks, Volume 7: Structural Analysis of Complex Materials*; Pergamon: New York, 2003.
(20) McGreevy, R. L. *Nucl. Instrum. Methods Phys. Res., Sect. A* **1995**, *354*, 1.
(21) Qiu, X.; Božin, E. S.; Juhas, P.; Proffen, T.; Billinge, S. J. L. *J. Appl. Crystallogr.* **2004**, *37*, 110.
(22) Goodenough, J. B.; Loeb, A. L. *Phys. Rev.* **1955**, *116*, 32.
(23) Orgel, L. E.; Dunitz, J. D. *Nature* **1957**, *179*, 462.
(24) Jahn, H. A.; Teller, E. *Proc. R. Soc. London, Ser. A* **1937**, *161*, 220.
(25) Wojtowicz, P. J. *Phys. Rev.* **1959**, *116*, 32.
(26) Felsenfeld, G. *Proc. R. Soc. London, Ser. A* **1956**, *236*, 506.
(27) Tackett, R.; Lawes, G.; Melot, B. C.; Grossman, M.; Toberer, E. S.; Seshadri, R. *Phys. Rev. B* **2007**, *76*, 024409.
(28) Suzuki, T.; Katsufuji, T. *Phys. Rev. B* **2008**, *77*, 220402.
(29) Yeo, S.; Horibe, Y.; Mori, S.; Tseng, C. M.; Chen, C. H.; Khachaturyan, A. G.; Zhang, C. L.; Cheong, S.-W. *Appl. Phys. Lett.* **2006**, *89*, 233120.
(30) Zhang, C. L.; Yeo, S.; Horibe, Y.; Choi, Y. J.; Guha, S.; Croft, M.; Cheong, S.-W.; Mori, S. *Appl. Phys. Lett.* **2007**, *90*, 133123.
(31) Sinha, A. P. B.; Sanjana, N. R.; Biswas, A. B. *J. Phys. Chem.* **1958**, *62*, 191.
(32) Buhl, R. *J. Phys. Chem. Solids* **1969**, *30*, 805.
(33) Robbrecht, G. G.; Henriet-Iserentant, C. M. *Phys. Status Solidi* **1970**, *41*, K43.
(34) Metz, R.; Caffin, J. P.; Legros, R.; Rousset, A. *J. Mater. Sci.* **1989**, *24*, 83.
(35) Gillot, B.; Buguet, S.; Kester, E. *J. Mater. Chem.* **1997**, *7*, 2513.

powder of the same composition in covered alumina crucibles. Pellets were water-quenched since single-phase $CuMn_2O_4$ forms in a very narrow temperature window between ~830 and 910 °C.[36] Laboratory X-ray diffraction (XRD) data were acquired on a Philips X'Pert diffractometer with Cu Kα radiation. Magnetic properties were measured using a Quantum Design MPMS 5XL SQUID magnetometer. Time-of-flight (TOF) neutron scattering was performed on the NPDF diffractometer[37] at Los Alamos National Laboratory. Rietveld refinement was performed using the XND code[38] for X-ray data and GSAS[39] for TOF data. The PDF and $F(Q)$ were extracted using the PDFGetN program,[40] and least-squares refinement of the PDF was performed using the PDFgui front end for PDFFit2.[41] We used $Q_{max} = 30$ Å^{-1} to construct $G(r)$, with selection criteria based on the peak-width methods of Qiu et al.[21] XPS spectra were acquired on sintered pellets using a Kratos Axis Ultra spectrometer. Peak fitting for XPS was performed using CasaXPS with a Shirley-type background and Gaussian peaks.

Reverse Monte Carlo (RMC) simulations[20,42] were run using RMCProfile version 5[43] on a 10 × 10 × 7 hausmannite supercell with 19 600 atoms. A hard-sphere repulsion was applied to prevent Mn−O and Cu−O bond distances of less than 1.79 and 1.82 Å, respectively. The fraction of random attempted swaps between Cu and Mn was kept at 5% of the translational moves. Runs were performed using a maximum translational step size of 0.02 Å, and the data set error, σ, was adjusted to reflect experimental uncertainty while maintaining a move acceptance probability of ~50%. A typical simulation was run for about 6 million steps and required ~12 h on a 2 GHz Intel Pentium 4 processor. Many starting configurations (disordered and ordered) were used to observe the progression of the simulation to similar final configurations. There were 2800 tetrahedra and 5600 octahedra, with Cu and Mn allowed to swap positions to attain the best fit to the total scattering function $F(Q)$ and to $T(r)$, which is a functionally equivalent renormalization of $G(r)$ that includes an additive r-dependent term that gives a linearly increasing baseline:

$$T(r) = 4\pi\rho r\left[G(r) + \left(\sum_{i=1}^{n} c_i\bar{b}_i\right)^2\right] \quad (2)$$

where ρ is the density (in atoms/Å^3) and c_i and $\bar{b}_i$ are the atomic fraction and corresponding neutron scattering length of each atom type i in the model. The total scattering structure factor $F(Q)$ describes the scattering in reciprocal space and is related to $S(Q)$ as

$$F(Q) = [S(Q) - 1]\left(\sum_{i=1}^{n} c_i\bar{b}_i\right)^2 \quad (3)$$

For a thorough examination of the functions used to describe total scattering data, see the review by Keen.[44] The experimental $F(Q)$ was convoluted with the supercell size and fit for $Q \leq 15$ Å^{-1}, while $T(r)$ was fit for $r \leq 11$ Å. A paramagnetic contribution to $F(Q)$was simulated by adding random spins with an average μ_{eff} value from SQUID magnetometry to the magnetic cations (all except Cu^+). The magnetic contribution does not have any appreciable affect on $G(r)$.

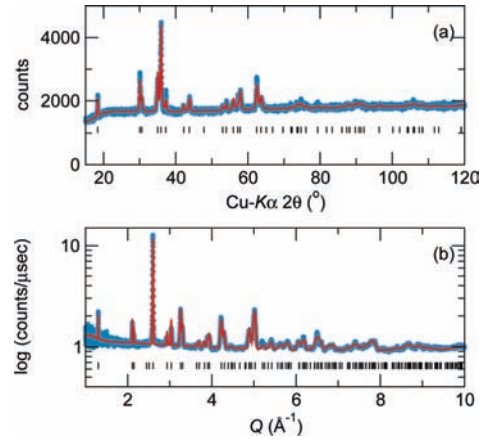

Figure 1. Rietveld refinement of single-phase, tetragonal $CuMn_2O_4$ from (a) laboratory X-ray diffraction data and (b) TOF neutron scattering data with $R_{wp} = 5.21\%$ acquired using the NPDF diffractometer at Los Alamos (note the log scale). Both data sets were collected at room temperature.

BVSs were extracted from atoms in the supercell using the bond valence formula

$$V = \sum \exp\left(\frac{R_0 - R_i}{0.37}\right) \quad (4)$$

where V is the cation valence, the sum runs over all bonds to the cation, the R_0 value for each cation−oxygen pair is tabulated in the work by Brese and O'Keeffe,[45] and R_i is the bond length (in Å). To assign an integer valence, V was calculated using each possible valence (1+ to 3+ for Cu and 2+ to 4+ for Mn), and the valence that most closely matched its corresponding V was assigned. Crystal structures were visualized with AtomEye[46] and VESTA.[47]

Results and Discussion

The laboratory Cu Kα XRD Rietveld refinement using the $I4_1/amd$ unit cell is shown in Figure 1a. The sample is single-phase, and all peak locations are matched by the tetragonal $I4_1/amd$ structural model. Although the first few peaks in the diffraction pattern are relatively narrow, indicating a significant crystalline correlation length, the counts die down rather quickly with increasing 2θ. The decline in counts is much quicker than would arise from the X-ray form factor falloff and is suggestive of large thermal displacement parameters. The Rietveld refinement of the highest-resolution bank (from four banks total) of TOF neutron powder diffraction data is shown in Figure 1b, and the corresponding structural parameters are given in Table 1. The extent of inversion was determined to be 0.270(2), and the structure was metrically tetragonal with $c/a = 1.03399(3)$. Neutron diffraction form factors are constants that are independent of the scattering angle and momentum transfer $Q = 2\pi/d$. Once again, the rapid decline of counts with Q is suggestive of large thermal displacement parameters, and this is indeed seen from the refinement results in Table 1. As we will describe presently, the large thermal parameters emerge from refinement of the Bragg scattering as a means of accommodating the varying coordination around the different

(36) Driessens, F. C. M.; Rieck, G. D. *Z. Anorg. Allg. Chem.* **1967**, *351*, 48.
(37) Proffen, T.; Egami, T.; Billinge, S. J. L.; Cheetham, A. K.; Louca, D.; Parise, J. B. *Appl. Phys. A: Mater. Sci. Process.* **2002**, *74*, S163.
(38) Bérar, J.-F.; Baldinozzi, G. *IUCr-CPD Newsl.* **1998**, *20*, 3.
(39) Larson, A.; Von Dreele, R. *Los Alamos Natl. Lab., Rep. LA* **2000**, *86*, 748.
(40) Peterson, P. F.; Gutmann, M.; Proffen, T.; Billinge, S. J. L. *J. Appl. Crystallogr.* **2000**, *33*, 1192.
(41) Farrow, C. L.; Juhas, P.; Liu, J. W.; Bryndin, D.; Bozin, E. S.; Bloch, J.; Proffen, T.; Billinge, S. J. L. *J. Phys.: Condens. Matter* **2007**, *19*, 335219.
(42) McGreevy, R. L. *J. Phys.: Condens. Matter* **2001**, *13*, R877.
(43) Tucker, M. G.; Keen, D. A.; Dove, M. T.; Goodwin, A. L.; Hui, Q. *J. Phys.: Condens. Matter* **2007**, *19*, 335218.
(44) Keen, D. A. *J. Appl. Crystallogr.* **2001**, *34*, 172.
(45) Brese, N. E.; O'Keeffe, M. *Acta Crystallogr., Sect. B* **1991**, *47*, 192.
(46) Li, J. *Model. Simul. Mater. Sci. Eng.* **2003**, *11*, 173.
(47) Momma, K.; Izumi, F. *J. Appl. Crystallogr.* **2008**, *41*, 653.

Table 1. Average Structural Parameters for $Cu_{1-\delta}Mn_\delta[Mn_{2-\delta}Cu_\delta]O_4$ [$\delta = 0.270(2)$] at 300 K Obtained from Rietveld Refinement of TOF Neutron Diffraction Data[a]

atom	site	*x*	*y*	*z*
Cu/Mn(tet.)	4*a*	0	$^3/_4$	$^1/_8$
Mn/Cu(oct.)	8*d*	0	0	$^1/_2$
O	16*h*	0	0.0272(1)	0.2629(1)

	U_{11}	U_{22}	U_{33}	U_{23}
Cu/Mn(tet.)	0.0116(5)	0.0116(5)	0.021(1)	
Mn/Cu(oct.)	0.0015(7)	0.0048(8)	0.020(1)	0.004(1)
O	0.0127(2)	0.0090(2)	0.0243(3)	−0.0095(3)

[a] $I4_1/amd$ (No. 141, origin choice 2), $a = 5.84755(8)$ Å, $c = 8.5508(3)$ Å, $c/a = 1.03399(3)$. All U_{ij} are given in Å^2.

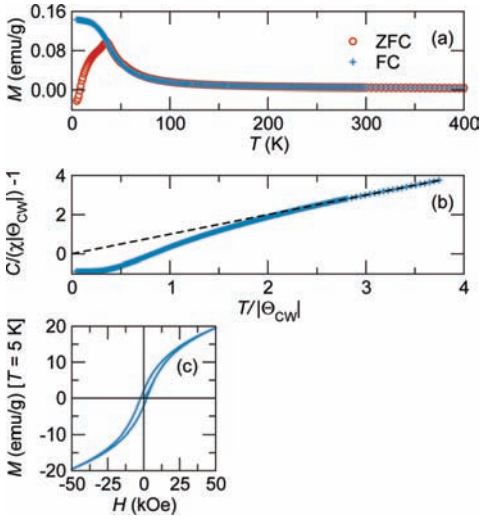

Figure 2. (a) Magnetization of $CuMn_2O_4$ after zero-field cooling (ZFC) and during field cooling (FC) acquired under a field of 100 Oe, showing the emergence of a hard ferrimagnet below 40 K. (b) Reduced molar susceptibility as a function of reduced temperature, with $C = 4.93$ emu K mol^{-1} Oe^{-1} and $\Theta_{CW} = -107$ K. The dashed line is the expectation for Curie−Weiss behavior. (c) Magnetization as a function of the magnetic field at 5 K.

cations on the tetrahedral and octahedral sites. Of particular interest is the anisotropy in the thermal parameters (data presented in Table 1).

In order to understand the nature of the magnetic interactions and ordering, temperature-dependent zero-field-cooled (ZFC) and field-cooled (FC) magnetization data for a well-characterized $CuMn_2O_4$ sample were recorded under a 100 Oe field (Figure 2a). The compound displays magnetic ordering to a ferrimagnetic ground state with diverging ZFC and FC magnetizations (indicative of a hard ferrimagnet) below $T_c = 35$ K. In Figure 2b, the reduced molar susceptibility is plotted as a function of the reduced temperature using the Curie constant *C* and the Curie−Weiss temperature Θ_{CW} obtained from fitting the high-temperature (320−400 K) portion of the molar susceptibility to the Curie−Weiss law, $\chi = C/(T - \Theta_{CW})$. The utility of such analysis in spinel compounds with magnetic ions at both the tetrahedral and octahedral sites has been presented elsewhere.[48] Deviations below the Curie−Weiss line (dashed) in such an analysis indicate long-range ferrimagnetism, corresponding to uncompensated antiferromagnetic coupling as the dominant

(48) Melot, B. C.; Drewes, J. E.; Seshadri, R.; Stoudenmire, E. M.; Ramirez, A. P. *J. Phys.: Condens. Matter* **2009**, *21*, 216007.

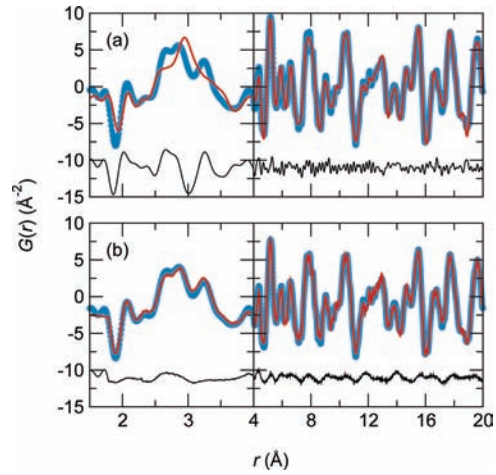

Figure 3. Fits to the experimental PDF for $r \leq 20$ Å via (a) least-squares refinement of a single unit cell and (b) RMC simulation using a 10 × 10 × 7 supercell. The *x*-axis scale has been stretched for $r < 4$ Å to emphasize the distinct local structure. Difference curves are shown at the bottom of each panel. The peaks from 2.5 to 3.5 Å describe O−O and B−B pair correlations. The nearest-neighbor Mn−O bonds (the negative peak at ∼2 Å) and the O−O correlations are not described by the $I4_1/amd$ model.

interaction. The extent of magnetic frustration, *f*, is equal to the ratio $|\Theta_{CW}|/T_c$, and this can be read as the inverse of the abscissa in Figure 2b. It is seen that $CuMn_2O_4$ is not very frustrated, perhaps because the antiferromagnetic interaction between the tetrahedral and octahedral sites is significantly stronger than other interactions. With many magnetic species in this compound, the single Curie constant *C* cannot be used to extract a consistent set of μ_{eff} values corresponding to the individual magnetic ions present. Figure 2c displays the magnetic hysteresis loop at 5 K for $CuMn_2O_4$, showing the absence of complete saturation even in fields of 50 kOe; this is a result of the site disorder in the compound.

We employed PDF analysis to probe the specific nature of the local deviations from the average structure. The noncooperative distortions are manifested in reciprocal space by diffuse scattering, which is converted via appropriate Fourier transformation of the total scattering $F(Q)$ into real-space distances of atom−atom pairs in the PDF. With the quality of data obtained on the NPDF diffractometer,[37] information on all real-space distances of atom−atom pairs up to lengths of ∼100 Å can be obtained. Experimental PDFs for $CuMn_2O_4$ are shown as points in the two panels of Figure 3. The least-squares-refined PDF (the solid line in Figure 3a) was obtained using the TOF Rietveld structure as input for PDFFit2 and provides an excellent fit to the large-*r* data ($r \gtrsim 4$ Å), but at shorter distances, the experimental PDF is very poorly modeled.

The poor fit for small *r* tells us which atom−atom pairs lead to the deviation between the average-structure model and the data. A noteworthy feature in the small-*r* PDF is the negative peak at 1.9 Å corresponding to Mn−O pairs; the peak is negative because Mn has a negative neutron scattering length. The average structure (solid line in Figure 3a) overestimates the Mn−O distance by ∼0.1 Å. Another significant mismatch between the data and the average-structure fit is seen in the cluster of peaks at 2.8 Å, which describe the O−O pairs on the edges of the polyhedra (tetrahedra and octahedra) and the B-site−B-site (B−B) pairs. Since neither the Mn−O nor O−O distances are well-fitted, the average structure does not describe the true local structure of the polyhedra in $CuMn_2O_4$.

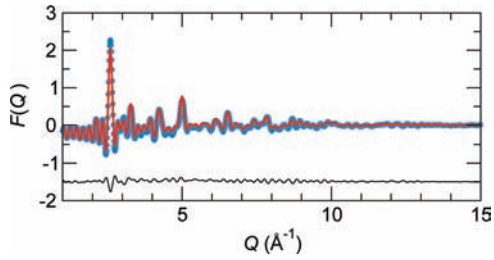

Figure 4. Fit to the experimental $F(Q)$ for $Q \leq 15$ Å^{-1} via RMC simulation. The data were convoluted to the width of the supercell. Fitting in reciprocal space simultaneously with $G(r)$ constrains the system to maintain a consistent average structure.

Single-cell PDFFit2 least-squares refinement of $CuMn_2O_4$ cannot produce a fit to the small-r region of the PDF while maintaining $I4_1/amd$ symmetry. Thus, the average symmetry is *not relevant within the unit cell.* To characterize the unit cell, we used RMC analysis, in which all of the atoms in the structure are allowed to translate freely, with constraints placed only on closest approach. It should be stressed that RMC simulations produce snapshots of plausible configurations that, taken in total, yield the locus of atoms that reproduce the data. Errors or artifacts in the data can manifest false structural details in the simulated structure, so properly normalized, high-quality data and an understanding of the origin of both systematic errors and true observed distortions is essential.[49]

RMC was performed as explained in Methods, and a typical fit to the PDF data for $CuMn_2O_4$ is shown in Figure 3b. The crucial difference between the PDF fits obtained by least-squares average-structure refinement and RMC simulation is the agreement of the latter with the data for the nearest-neighbor Mn−O and Cu−O bonds near 2 Å and the O−O and B−B clusters from 2.5 to 3.0 Å. At larger r, the number of contributing atoms increases as r^3, so the experimental $G(r)$ approaches the average structure.

The supercell of 700 unit cells can be folded back into a single unit cell to verify that the atoms are in reasonable positions that correspond to those of hausmannite. The fit to $F(Q)$ in Figure 4 helps keep this long-range structure in place. The folded configuration in Figure 5a has clusters of 700 atoms at each site. The RMC simulations allowed site-swapping of cations and produced a model with an inversion of $\delta \approx 0.35$, which is close to the value of 0.270 obtained from the Rietveld refinement. A key distinction between the least-squares refinement of the PDF and the fits obtained from RMC analysis is that peak broadening in the former is accommodated by instrumental broadening and thermal parameters. In contrast, RMC performs no such broadening, and broad $G(r)$ peaks can only be represented in the supercell by having an equally broad distribution of bond distances. RMC also does not account for termination ripples in $T(r)$ from the step function at $S(Q_{max})$. We therefore expect there to be some bond distances that are intuitively too long or short but still necessary in order to fit the systematic peak broadening inherent in every experimental PDF.

If the thermal displacement is isotropic, the distribution of atoms around each ideal lattice position should be spherical. This is not the case for the oxygen distributions, which were found (even in the TOF Bragg refinements) to be smeared

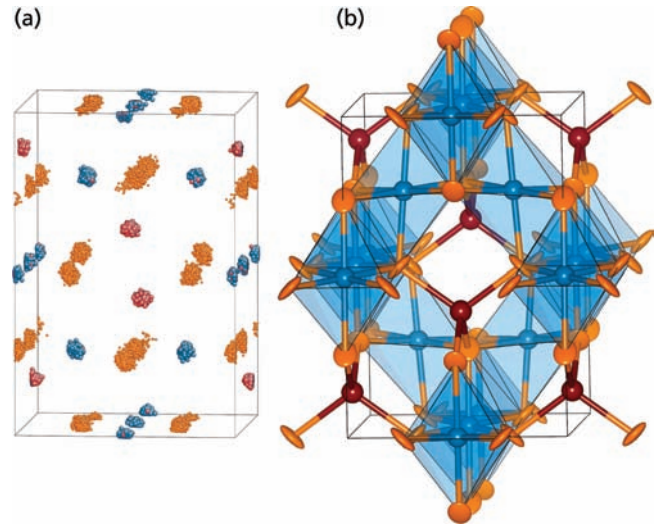

Figure 5. (a) "Point clouds" of simulated atom positions obtained by folding the 10 × 10 × 7 RMC supercell into a single unit cell. Color key: blue, Mn; red, Cu; orange, O. (b) Rietveld-refined unit cell with tetrahedral M−O bonds and coordination polyhedra around the octahedral sites; 95% thermal ellipsoids are depicted around O atoms. The O ellipsoids are highly oblate ($U_{23} < 0$), and the volume they trace roughly corresponds to the smearing of O positions in the RMC simulation. We stress that the RMC model need not perfectly reproduce the thermal ellipsoids since it describes noncorrelated local distortions.

normal to the tetrahedral M−O (M = Cu, Mn) bonds, resulting in a large value for U_{33} and a negative value for U_{23}. The oxygen clouds seen in Figure 5 are clearly nonspherical and should roughly lie within the long-range thermal displacement U factors. The comparison with the refined TOF Bragg data with $U_{23} < 0$ is shown in Figure 5b. The flattening of the oxygen point clouds toward the tetrahedral bonds is clearly evident in both fits.

We were able to separate the RMC distributions of Cu and Mn nearest-neighbor bond lengths on the basis of coordination and then plot the local environments for the cations. The distribution is shown in Figure 6. For a local structure that matches the average long-range structure perfectly, we would expect the Mn−O and Cu−O bond distributions at each site to be identical. Instead, Figure 6b clearly shows that nearest-neighbor Cu−O and Mn−O bond length peaks are centered distinctly apart from the average structural distance obtained from the Rietveld analysis. Indeed, we should assume that Mn and Cu in the same coordination environment would possess different bond lengths. Without a local structure probe such as PDF, these differences cannot be seen if they lack long-range cooperative ordering.

Bond angles can also be separated by cation and coordination and extracted from the RMC supercell. The O−M−O bond angle distributions $B(\theta)$ in Figure 7 are weighted by $\sin(\theta)^{-1}$ to account for the probability of finding a given angle θ for a randomly rotated bond.[50] The bond angles from the average $I4_1/amd$ structure are denoted by the vertical lines in Figure 7e. The O−Cu−O bond angles in Figure 7a display a clear bimodal difference curve when fit to a single Gaussian, and the fit can be improved significantly by fitting to two Gaussians with centers at 107.1 and 111.9° (Figure 7b), which are more distorted than the Rietveld values of 108.0 and 110.2°. These two angles

(49) Peterson, P. F.; Bozin, E. S.; Proffen, T.; Billinge, S. J. L. *J. Appl. Crystallogr.* **2003**, *36*, 53–64.

(50) Tucker, M. G.; Keen, D. A.; Evans, J. S. O.; Dove, M. T. *J. Phys.: Condens. Matter* **2007**, *19*, 335215.

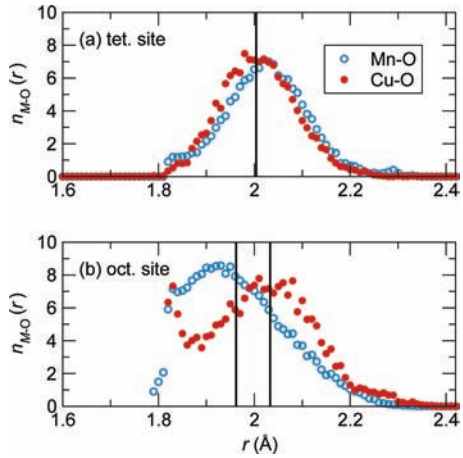

Figure 6. Partial bond distance distributions $n_{M-O}(r)$ for (a) tetrahedral and (b) octahedral M−O pairs obtained from RMC modeling of $CuMn_2O_4$ according to cation species and coordination. Some clustering is seen near the hard-sphere cutoff and is a result of RMC fitting to the small-r termination ripples. Average-structure bond lengths from the Rietveld refinement are denoted by vertical lines. The average structure would contain four short and two long octahedral bonds in (b), but this is not seen in the RMC results.

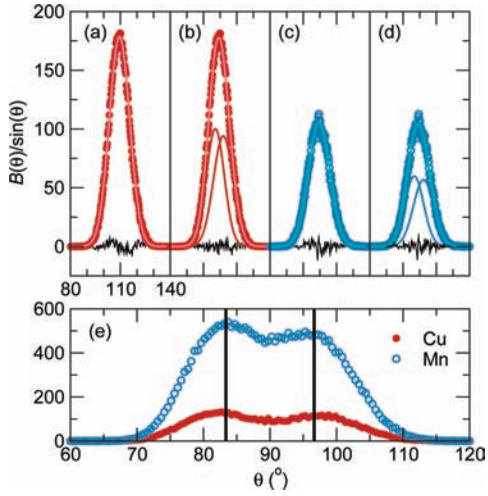

Figure 7. Bond angle distributions $B(\theta)$ for all nearest-neighbor O−M−O bond angles in the RMC simulation for (a, b) tetrahedral Cu ions, (c, d) tetrahedral Mn ions, and (e) octahedral ions. Average-structure (Rietveld) bond angles are shown by vertical lines. In (a) and (c), the data were fit using a single Gaussian. In (b) and (d), two Gaussians centered equidistant from 109.5° were used. The χ^2 value for O−Cu−O tetrahedral angles was improved from 47.0 to 31.5 by fitting to two peaks, but that for O−Mn−O was only improved from 48.8 to 41.6.

angles correspond to a flattening of the coordination around tetrahedral copper. As Figure 7c,d shows, fitting O−Mn−O bond angles with a single Gaussian does not produce a bimodal difference, and the improvement after fitting to two angles is not as marked as for the Cu tetrahedra. This evidence points toward MnO_4 tetrahedra that are significantly less distorted than the CuO_4 ones. Distortions of tetrahedral Cu^{2+} are known in systems where the tetrahedra do not share features (e.g., in compounds with isolated CuX_4^{2-} species).[51] The literature on distorted Cu^{2+} tetrahedra in extended oxides is more scarce.[52]

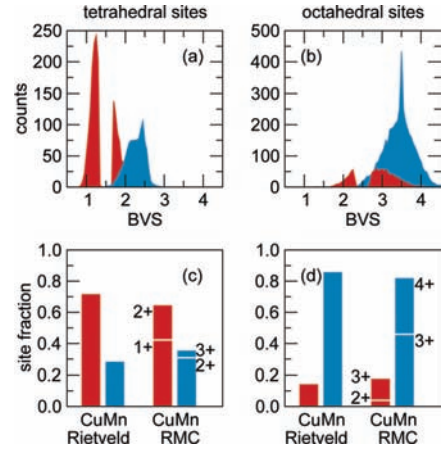

Figure 8. Histograms of bond valences for (red) Cu and (blue) Mn calculated on the (a) tetrahedral and (b) octahedral sites from the M−O bond length distributions of the RMC supercell. In (c) and (d), the fractions of Cu and Mn on the two sites calculated from the Rietveld refinement are compared with the statistical RMC results in (a) and (b), respectively. The tendency for charge disproportionation away from Cu^{2+} and Mn^{3+} and the presence of octahedral Cu^{3+} should be noted.

The bond angles of MO_6 octahedra in Figure 7c show a two-peak distribution centered near 80 and 100°. Describing the MO_6 shape from the bond angle distribution is more complex than in the tetrahedral case, but we expect there to be *less* cation-dependent distortion on the B site because of edge sharing between octahedra. In contrast, no tetrahedra share edges or corners with one another.

Just as bond distances and bond angles can be obtained from an RMC snapshot, bond valence sums can be calculated for each cation. Because we applied no symmetry constraints in the RMC analysis, bond distances and nearest-neighbor information are truly local and not influenced by long-range ordering in the bulk. Valence states for each cation were assigned by minimizing the difference between the ideal and BVS-calculated valence sums using the RMC bond distances. These distributions are shown in Figure 8, both as distributions of the calculated BVS for each cation of each coordination (top) and stacked bar charts comparing the inversion and charges for Rietveld versus RMC results (bottom). Inversion of Mn onto the A site and the presence of d^{10} Cu^+ and d^5 Mn^{2+} both serve to dilute the cooperative JT effect. Analysis of the bond valence of the RMC snapshots reveals that *only 28% of the tetrahedral cations* are JT-active d^9 Cu^{2+} or d^4 Mn^{3+}.

On the basis of the average bond distances from the Bragg refinement, the valences of the Cu ions on the tetrahedral and octahedral sites are 1.66 and 2.63, respectively. These do not agree with the RMC results, which have the majority of tetrahedral Cu as Cu^+. The average structure also finds Mn valences of 2.07 and 3.27 for the tetrahedral and octahedral sites, respectively. While the RMC simulations do indeed find tetrahedral Mn to be mostly Mn^{2+}, the octahedral Mn is 55% Mn^{3+} and 45% Mn^{4+}. Our RMC BVS results give a cell with a valence of 1.63+ on the A site and 3.33+ on the B site. This is a total cation valence of 8.29+ in the formula unit, which very close to the value of 8+ expected for $CuMn_2O_4$ despite the fact that no constraints on the total charge were imposed in the simulation. The total cation valence for the average Rietveld structure was only 6.9+.

(51) Greenwood, N. N.; Earnshaw, A. *Chemistry of the Elements*, 2nd ed.; Butterworth-Heinemann: London, 1997.
(52) Day, M. C.; Selbin, J. *Theoretical Inorganic Chemistry*; Reinhold: New York, 1962.
(53) Steiner, P.; Kinsinger, V.; Sander, I.; Siegwart, B.; Hüfner, S.; Politis, C.; Hoppe, R.; Müller, H. P. *Z. Phys. B* **1987**, *67*, 497.

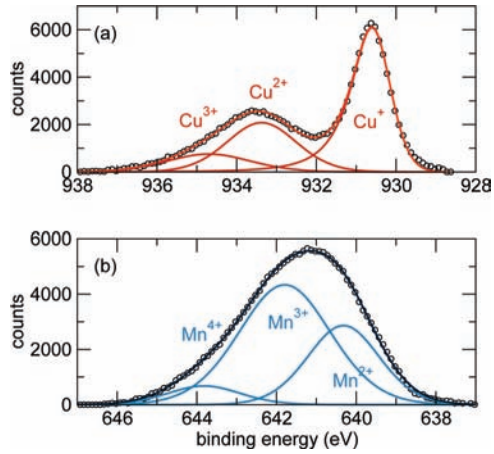

Figure 9. XPS spectra for the $2p_{3/2}$ regions of (a) Cu and (b) Mn cations provide another probe of the mixed valences. Most important is the unambiguous Cu^+ peak at 934.8 eV, in agreement with the BVS analysis, and the Cu^{3+} peak assigned on the basis of energy shifts from a comparison between CuO and $NaCuO_2$.[53]

Table 2. Stoichiometric Amounts per $CuMn_2O_4$ Formula Unit of the Different Charge States at the Different Sites Suggested by Bond Valence Sum (BVS) and XPS Results[a]

	Cu			Mn		
charge	tet. (BVS)	oct. (BVS)	XPS	tet. (BVS)	oct. (BVS)	XPS
1+	0.42 (42%)		47%			
2+	0.20 (20%)	0.10 (10%)	35%	0.34 (17%)		35%
3+		0.28 (28%)	18%	0.05 (2%)	0.89 (44%)	47%
4+					0.72 (36%)	18%

[a] Values in parentheses are percentages of total numbers in the formula unit. The percentage values obtained from integrated areas of the XPS signals are insensitive to the coordination.

Interpretation of the Cu $2p_{3/2}$ XPS spectra in Figure 9a reveals most readily the large Cu^+ peak at 930.6 eV, which is confirmed by BVS analysis of the RMC supercell to be entirely confined to the tetrahedral sites. Prior XPS studies of $CuMn_2O_4$ have found the same Cu^+ peak for similar heat treatments, and the typical proposed ionic configuration is $Cu_{0.76}{}^{+}Mn_{0.24}[Cu_{0.24}{}^{2+}Mn_{1.76}]$, in which the tetrahedral Mn can be Mn^{2+} or Mn^{3+} and the octahedral Mn balance this with a combination of Mn^{3+} and Mn^{4+}.[32,54−56] One key distinction between the prior XPS results and those of the BVS is the appearance of B-site Cu^{3+} in the RMC supercell. The broad peaks at 933.4 and 934.75 eV have in the past been assigned to octahedral and tetrahedral Cu^{2+}, respectively.[54,57] However, we note that the shift of ~1.3 eV between these two peaks is the same as that between Cu and Cu^{3+} in CuO and $NaCuO_2$.[53] It is therefore possible that the highest-energy peak, which was previously assigned to tetrahedral Cu^{2+}, is actually that of octahedral Cu^{3+}.

Table 2 compares the distributions of the different ions in their different charge states, as suggested by the bond valence analysis of RMC metal−oxygen distances, with the integrated areas under the different XPS peaks. While the stoichiometric amounts of Cu^{2+} and Mn^{3+} in the formula units as obtained from the BVSs closely match the suggested relative amounts from XPS, for the lower- and higher-valent states of both Cu and Mn, the correspondence is less impressive. A more quantitative spectroscopic study may thus be needed.

Conclusions

We have demonstrated that an ostensibly simple extended compound, $CuMn_2O_4$, is structurally very complex as a consequence of incoherent Jahn−Teller distortions and multiple valence states of the two cations in conjunction with site disorder. The particular sample examined was tetragonal, quenched from high temperatures, and characterized by near 30% inversion. The compound underwent glassy magnetic ordering near $T_c = 35$ K to give an unsaturated ferrimagnetic state. Using a combination of neutron scattering, RMC simulations, and tools used to examine glass structures, we have been able to develop a consistent picture of the structure (or more accurately, the positional tendencies of atoms) of a compound that has long provided a challenge to structural and spectroscopic tools. Some of the findings are surprising. Using details of the neighboring metal−oxygen distances and bond valence calculations, we have ascertained that the compound tries to minimize the population of JT-active ions on the tetrahedral site, implying Cu charge disproportionation according to

$$2Cu^{2+} \rightleftarrows Cu^{+} + Cu^{3+}$$

A similar disproportionation takes place with Mn^{3+}, for which both the lower and higher charge states are JT-inactive. It is rare to observe stabilization of Cu^{3+} or other high-valence cations in the spinel structure. Normally, one expects to find Cu^{3+} only in oxides with highly electropositive cations (e.g., $ACuO_2$, where A is an alkali cation from Li through Cs).[58,59] In the spinel, stabilization is achieved because Cu in an octahedral environment can move to a d^8 Cu^{3+} configuration. These octahedra resist breaking Pauling's third rule: they need not share edges with each other, since less than one in six octahedral cations is Cu^{3+}.

This is the first time that bond valence has been used to suggest the presence of Cu^{3+} in $CuMn_2O_4$, and this suggestion finds support from X-ray photoelectron spectroscopy: features in the core-level XPS spectra of Cu that were previously attributed to differences in coordination may rather be due to differences in valence state. The use of bond valence in a compound with mixed site occupancies is itself unusual and becomes possible because the modeling allows a statistical analysis of the coordination and bond lengths. Finally, for the first time, it is noted that presence of a large fraction of Cu^{2+} results in the tetrahedra being somewhat flattened, also in an incoherent manner. It is germane to point out that the spinel tetrahedral sites form a diamond lattice, and these are notoriously hard to distort; this has been well-studied in the related system of Kagomé lattices.[60] Indeed, in the diamond lattice formed by considering only the average positions of the tetrahedral cations, all of the cation−cation distances in $CuMn_2O_4$ are equal.

Extracting statistical information from large-box modeling of disordered crystalline materials remains a burgeoning field with many open questions. For example, it remains to be seen whether there is evidence for valence-specific local distortions in $CuMn_2O_4$. Future studies may, as an example, utilize powerful geometric analysis algorithms to describe

(54) Lenglet, M.; D'Huysser, A.; Kasperek, J.; Bonnelle, J.; Durr, J. *Mater. Res. Bull.* **1985**, *20*, 745.
(55) Beley, M.; Padel, L.; Bernier, J. C. *Ann. Chim.* **1979**, *3*, 429.
(56) Vandenberghe, R. E.; Robbrecht, G. G.; Brabers, V. A. M. *Phys. Status Solidi A* **1976**, *34*, 583.
(57) Porta, P.; Moretti, G.; Musicanti, M.; Nardella, A. *Solid State Ionics* **1993**, *63−65*, 257.
(58) Hestermann, K.; Hoppe, R. *Z. Anorg. Allg. Chem.* **1969**, *367*, 249.
(59) Berger, R.; Tergenius, L. *J. Alloys Compd.* **1994**, *203*, 203.
(60) Guest, S. D.; Hutchinson, J. W. *J. Mech. Phys. Solids* **2003**, *51*, 383.

continuous symmetry measures of a particular polyhedral distortion.[61,62] Efforts are also under way to incorporate more data and constraints in each RMC simulation, such as the X-ray $F(Q)$ and Bragg profile or EXAFS, NMR, or EPR data. With so much information within the supercell, the task will be to create well-defined metrics of local distortions and ensure that their presence is statistically supported by multiple simulations.

Acknowledgment. The authors thank Katharine Page, Thomas Proffen, Andrew Goodwin, and Matthew Tucker for extensive discussions. This work has benefited from the use of the NPDF diffractometer at the Lujan Center at Los Alamos Neutron Science Center, funded by the DOE Office of Basic Energy Sciences. Los Alamos National Laboratory is operated by Los Alamos National Security LLC under DOE Contract DE-AC52-06NA25396. This work was supported by the Institute for Multiscale Materials Studies, the donors of the American Chemical Society Petroleum Research Fund, and the National Science Foundation through a Career Award (DMR 0449354) to R.S. Use of NSF MRSEC facilities (DMR 0520415) is acknowledged.

JA902096H

(61) Pinsky, M.; Avnir, D. *Inorg. Chem.* **1998**, *37*, 5575.

(62) Alvarez, S.; Alemany, P.; Casanova, D.; Cirera, J.; Llunell, M.; Avnir, D. *Coord. Chem. Rev.* **2005**, *249*, 1693.